# Fractographic Study to Characterise the Interaction Between Intralaminar and Interlaminar Fracture From Embedded Defects Under Compression Loading

Carla Canturri[1], Emile S. Greenhalgh[†2], Leif E Asp[3], Silvestre T Pinho[2],

[1]Singapore Institute of Manufacturing Technology, Singapore 637662

[2]Composites Centre, Imperial College London, South Kensington, London, SW7 2AZ

[3]Chalmers University of Technology, 412 96 Göteborg, Sweden

[†]Corresponding Author

Abstract

This paper describes the fractographic observations from the study of embedded defects subject to compression. The fractographic observations aim to characterise the interaction between intralaminar and interlaminar fracture and to understand their role in the delamination growth and the delamination migration. The influence of the stacking sequence orientation on the damage modes is studied in eight different configurations. A detailed fractographic study led to the identification of the different failure modes and failure sequence. It was also possible to establish the stacking sequences more prone to delamination migration and the failure modes more critical for damage tolerance.

## 1. Introduction

Delamination has been recognised as the principal damage process in laminated composites under compressive and bending loading conditions [1]. When such delaminations propagate in a structure, large reductions in performance can result [1]. Delaminations can develop from a number of features such as ply-drop-offs, notches or inclusions. Also, most critically, delamination is one of the principal failures modes following low velocity impact. The

sensitivity of composite components to delamination is perhaps the key driver for the need to "make and test" for composite certification.

A particular defect which has been widely studied to investigate delamination behaviour is the embedded single-plane defect under compressive loading [2–6]. Such defects are representative of manufacturing defects which may have been introduced during fabrication of composite structures. A further motivation for studying such defects has been the simplification of the damage state induced by low velocity impact damage [7]. However, a comparative study using post-buckled stiffened panels [8] concluded that the damage growth mechanisms for these two defects are fundamentally different: impact damage induces a localised perturbation of the laminate, which then bends as the compressive loading is applied, driving rapid delamination growth and culminating in a 'notched' flexural failure. For embedded defects closer to the outer faces, the delamination growth tends to be stable (i.e. not global bending driven), and consequently a very different behaviour ensues.

It has been recognised [9–16] that *delamination migration* is a critical phenomenon in understanding how delaminations grow within a laminate or structure: this is the process by which the delamination crack will change between ply interface as it extends. Delamination migration has been studied statically and in fatigue by means of single cantilever beams [15], end-load-split beams [16] and double-clamped asymmetric beams which permitted the isolation of a single migration event [9,10]. The authors [12,14,17] have also demonstrated migration using a tapered width cantilever beam. A key observation from these studies is that the orientation of the driving force for delamination growth with respect to the local ply orientations at the delaminated interface is critical to the migration processes that ensue [14]. Characterisation of the behaviour of laminates containing embedded single plane delaminations can be viewed as the next step in complexity in the study of delamination migration.

In previous studies in this area, a plate or slender coupon containing a pre-implanted insert was subjected to either compressive [2,3] or bending loads [6]. These studies have demonstrated that delamination growth from the pre-implanted insert is controlled by the insert depth and laminate stacking sequence, and is relatively insensitive to defect shape and size (unless higher local buckling modes develop) [2]. The fracture mechanisms observed from such tests illustrate the complexity of the problem: despite the external appearance of a continuous crack front, a single plane defect usually results in multiplane delamination growth, intralaminar splitting and even fibre fracture [6,8,18].

The complexity of the processes associated with delamination growth have a profound influence on damage tolerant design, since identifying the conditions under which rapid damage growth will occur (i.e. safety critical conditions) and conditions under which benign growth will develop (i.e. benevolent growth conditions), is imperative. The means to distinguish between these conditions is through understanding the detailed (local) growth processes, and how they interact, hence dictating global damage propagation and ultimately loss of load carrying capability. The aforementioned delamination migration phenomenon underpins this understanding: if there is migration, it can lead to bridging of fibre bundles across the crack faces, thus inhibiting further delamination extension. Conversely, if the delamination reaches a critical plane in which it will not migrate, then damage growth is rapid.

In this paper, the influence of the orientation of the plies at a pre-existing delaminated interface (i.e. an embedded defect) with respect to the applied loading on the damage growth mechanisms is investigated. An experimental procedure has been developed to investigate the failure modes while progressively changing the ply orientation at the defect plane to characterise their influence on delamination migration, and hence the damage development. Understanding these damage growth processes is key to damage tolerant design: i.e.

identifying under which fracture processes migration, instead of rapid damage growth, develops. The overarching focus of the paper is to use fractography to understand the failure processes in these specimens, and hence provide validation data for the development of physically based predictive models of delamination growth.

## 2. Experimental Methods

### *2.1. Specimen Preparation*

Three 620 mm x 620 mm laminates were fabricated using a quasi-isotropic stacking sequence, $[+45^{\circ}/-45^{\circ}/0^{\circ}/90^{\circ}]_{4s}$, manufactured from Cytec HTA/919 unidirectional tape (0.125mm thick) and autoclave cured following the manufacturer's recommendations [19], to give a nominal laminate thickness of 4.2mm. The laminates were manufactured containing 10μm thick circular PTFE film defects, of 50mm diameter, between the third and fourth plies from the back face (i.e. a 0°/90° ply interface). Following fabrication and ultrasonic inspection to accurately identify the positions of the embedded defects, eleven 250 mm x 150 mm plates were cut from the laminates, with the longer edge orientated at 0˚, 90˚, 87˚, 85˚, 80˚ (2 specimens), 75˚, 70˚, 65˚ (2 specimens) and 45˚ with respect to the 0° plies. This resulted in the defects being located at the ply interface angles tabulated in Table 1. The plates were cut such that the embedded defects were located at the centre of each specimen. Details of the nomenclature used for the specimens and the numbering system are given in Figure 1 and Table 1.

Following cutting, a 1 mm hole was partially drilled through the front face through to the centre of the delamination plane to ensure the air pressure was equalised during local buckling [20]. Steel end tabs (150 mm x 50 mm) were adhesively bonded on the specimens giving a gauge section of 100 mm in length and leaving the lateral edges free. Two strain gauges (Figure 1) were attached on either side of the delamination to detect global buckling

and to ensure uniform loading. Specimens were tested in quasi-static compression, at a stroke speed of 0.5 mm/min applied parallel to the longer specimen edge (but not necessarily parallel to the 0° ply). The applied compressive displacement of the specimen, $\delta$, and the out-of-plane displacement of the front ($v_f$) and back ($v_b$) faces at the specimen centre were measured using laser and dial gauges. From monitoring the in-plane/out-of-plane displacement response, the local and global buckling loads of the specimens were identified, although the former only had a resolution of kilonewtons. Testing was conducted using a series of loading steps. The steps were determined during each test: loading was interrupted whenever macroscopic delamination growth could be determined visually or acoustically. After macroscopic delamination growth, the specimens were unloaded completely and removed from the testing machine. Ultrasonic inspection (time of flight) of the specimens to gauge the extent of the delamination growth entailed removal of the specimen from the loading fixture, ultrasonic inspection using immersion to characterize the damage extent, and then drying. The subsequent loading steps were determined in a similar manner.

## 2.2 Fractographic Analysis

To characterise the damage mechanisms, five specimens (indicated in bold on Table 1) were chosen for detailed fractographic inspection. The specimens were selected to represent a diverse spectrum of ply interfaces: specimen B (90°/0°), specimen C (+87°/-3°), specimen E2 (+80°/-10°), specimen H2 (+65°/-25°), and specimen I (+45°/-45°), with the latter deemed to be the Baseline specimen. To expose the delamination fracture surfaces, the surface layers were carefully cut away using a hand-held ‘Dremel’ type circular saw. Following dissection, the fracture surfaces were imaged on a flatbed scanner. Then both matching surfaces were mounted on stubs, gold sputter coated for 30 seconds and examined under an S-3400N Hitachi scanning electron microscope (SEM) and a Leo 1550 Field Emission Scanning Microscope (FE-SEM) at magnifications between x40 and x1000 with an acceleration

voltage of 15 kV. Regarding the ultrasonic scans, only the fracture surfaces associated with the mechanical test (and not any artefacts from the dissection) were characterised. From inspection of these fracture surfaces, the failure modes, damage growth directions and delamination failure sequences were inferred. Micrographs were taken from the front matching (Figure 3) surface except Figure 8 and Figure 9 that were taken at the back matching surface (Figure 3)

## 3. Mechanical Test Results

The results of the mechanical tests are summarised in Table 2, which show the maximum applied load, delamination initiation strains, and global and local buckling loads. Note that this data was associated with testing for the first load step, i.e. after local/global buckling and after the delamination was visually observed to have grown. A typical load/out-of-plane displacement and respective load/front and back strains (specimen I) are shown in Figure 2. Local buckling was deduced from the divergence of the front face out-of-plane displacement from that of the back face out-of-plane displacement (see Figure 2), whilst the global buckling was deduced by simultaneous divergence of both the back and front face in-plane strains.

All specimens, except Specimen B (90°/0°), presented significant, stable, delamination growth. The general sequence of failure was as follows, as illustrated in Figure 3: firstly, local buckling occurred (Figure 3a) (i.e. buckling of the sub-laminate immediately above the insert), which was then followed by global buckling of the entire specimen (Figure 3b). Following this, delamination initiation, and subsequent growth occurred at the transverse boundary (Figure 3c). The extent of the delamination growth could only be deduced from the C-scans between interrupted tests (Figure 4). Specimen B, however, presented catastrophic

compressive failure immediately upon initiation of delamination growth, with no local buckling having been evident.

From the tests it was observed that the global buckling loads were less than 2.5% lower than the maximum load. The local buckling load varied between 22 and 56 % of the maximum load during the first load step. For the second and third loading step this varied between 3 and 16 %. Also the maximum loads during the second and third load steps were almost the same as during the first load step. Finally, no significant dependency in strain for the onset of delamination growth with fibre orientation could be determined. After three load steps migration of the delamination determined via C-scan inspection was observed in all the specimens (Figure 4).

The effect of delamination growth on the mechanical performance of the panels was assessed by considering the reduction in effective load carrying capacity, i.e. the load at which global buckling was detected, in subsequent load steps (Figure 5a). The global buckling loads across all panels were combined and plotted against the relative damage growth occurred at the previous load step. The delamination growth was measured from the C-scans performed after each load step considering the combined delaminated area for all delaminated ply interfaces and normalised by the initial delamination area ($A_0$) so that the delamination growth (%)= $((A- A_0)/A_0)$. Note that the area thus measured is a lower bound estimate as ultrasonic C-scans are not able to capture delaminations growing concurrently at two different ply interfaces. However, the fractographic analysis (Section 4) showed that the delaminations had mainly propagated at a single ply-interface.

In Figure 5a, *previous delamination growth* refers to the pre-existing delamination at the moment to initiate the test. For example: the delamination growth achieved during the second load step was plotted against the global buckling load at the third load step. The results

(Figure 5a) show little correlation between the delamination extent and the load at which the panel experienced global buckling. However, when the global buckling load is compared with the maximum load of the previous load step a stronger correlation was found Figure 5c. This could indicate that the presence of other failure modes observed fractographically may have stronger effects in the panel performance.

The delamination growth extent was also analysed in terms of the back ply angle (Figure 5b). In this case the delamination growth $((A- A_0)/A_0)$ was normalised by the maximum load attained per each load step. As the tests were interrupted at different load levels, which had an effect on the delamination growth extent (delamination growth (%)), it was necessary to normalise the delamination growth with the maximum load attained at each load step (Max load (kN)) to be able to compare between different load steps. It could be seen that although initial delamination growth was insensitive to the orientation of the back ply, at the second and third load step, panels B, D, E2 and F presented extensive delamination growth and in one case reaching the edges of the specimen (denoted *until free-edge* in Figure 5b).

## 4. Fractographic Observations

In the following paragraphs the detailed observations from the fractographic studies are reported. For clarity, the detail of the Baseline (Specimen I; +45˚/-45˚ ply interface) is described and then the differences between the Baseline and subsequent specimens are presented. It should be noted that visual inspection of the exposed delamination surfaces identified tide marks [21] which matched the delamination fronts seen in the C-scans [22].

### *4.1. Observations on Specimen I (+45˚/-45˚ ply interface) - Baseline*

Firstly, consider the Baseline specimen (Specimen I) which had a stacking sequence of $[90˚/0˚/+45˚/-45˚]_{4s}$, with the initial defect at the +45°/-45° ply interface (Figure 6). In this, and subsequent images for the other specimens, the C-scan of half the delaminated portion

from the end of the test (Figure 6a), an optical image of the equivalent delamination surface (Figure 6b) and a schematic of the delamination surface indicating the ply interfaces (Figure 6c), are shown. Visual inspection of the delamination surface of Specimen I (Figure 6b) identified long intralaminar splits in the third (+45˚) and second (0˚) plies and delamination migration. The delamination migration was driven towards the back face of the specimens and two migrations were observed. It has been shown by the authors in [14], that delamination migration is driven by the sign of the shear at the delaminating interface. In this configuration and for compressive loading, the resolved shear stresses at the transverse boundary, indicate that the delamination migration will be driven towards the back face. The ply towards which delamination migration is being driven is identified by means of an underline in the micrographs. The shear stresses at the transverse boundary (Figure 3c) arise from the difference between the transverse deformations of the back and front sublaminates. There were imprints of these ply splits on the matching surfaces of the fourth ply, from which it was inferred that these ply splits had occurred before delamination between the third and fourth plies.

Scanning electron microscopy presented evidence of further small ply splits in the third ply (+45°) adjacent to the insert boundary. Figure 7 shows detail of the delamination growth initiation from the insert boundary (site 1 in Figure 6c); fibre imprints from the third ply (+45˚) whilst the fibres of the fourth ply (-45˚) are visible underneath. From the tilt of the cusps it can be inferred that the growth had extended from the insert [23]. Figure 8 (site 2 in Figure 6c) shows the delamination morphology further around the insert boundary. The continuity of the delamination morphology across the ply splits in the third ply was consistent with the delamination having occurred prior to ply splitting in this region. The delamination growth had been mode I dominated in this region on the insert boundary.

Moving away from the starter defect in the direction of delamination growth, there was evidence of fibre fracture having occurred. Figure 9 (site 3 in Figure 6c) was at the intersection of a region containing +45° fibre compression failure, 0° fibre in-plane shear failure and ply splits A-A' and B-B' (Figure 6c). These ply splits acted as initiation sites for the 0˚ shear failure presented in Figure 9. This in-plane shear failure then transformed into a 0˚ compression failure until reaching ply split C-C' (Figure 6c) in the second (0˚) ply. Since the fibre failure of the second ply was confined between these two ply splits (A-A' and B-B' in Figure 6c) it was inferred that these two intralaminar failures had occurred prior to fibre failure.

Based on the fractographic observations, the sequence of failure of the Baseline (Specimen I) which had a defect at the +45°/-45° ply interface can be summarised as follows (Figure 10). As shown in Figure 10a, once the delaminated plies above the starter defect had locally buckled, intralaminar failure had developed in the plies which had been subjected to larger bending strains (i.e. the third ply: +45°). Hence, once the delamination had started propagating within the original defect plane (Figure 10b), numerous ply splits were already present in the third ply which had led to delamination migration into the adjacent $2^{nd}/3^{rd}$ ply interface (0°/+45°). Further migration of the delamination plane had occurred via the 0° ply split B-B' (Figure 6) into the interface between the first and second plies (90°/0°), as shown in Figure 10c. As a consequence of this delamination, the exposed second ply (0˚), leading to out-of-plane microbuckling and compression failure (Figure 10c).

### *4.2. Observations on Specimen H2 (+65˚/-25˚ ply interface)*

The next configuration studied (Specimen H2) had a stacking sequence $[-70^{\circ}/+20^{\circ}/+65^{\circ}/-25^{\circ}]_{4S}$: i.e. it was rotated +20˚ with respect to the Baseline, such that the initial defect was located at a +65˚/-25˚ ply interface. As can be seen in Figure 11, this specimen exhibited three long ply splits (labelled A-A', B-B' and C-C' in Figure 11c) in the third ply which had

resulted in migration of the delamination to the adjacent +20˚/+65˚ ply interface (i.e. between the second and third plies). Splits A-A', B-B' and C-C' had led to a change of the delamination growth interface. Similarly to Specimen I, these ply splits had formed prior to the delamination growth, and hence provided a path by which the delamination migrated. These ply splits, however, were not sufficient for delamination migration as can be seen in Figure 12 (site 4 in Figure 11) in which the ply split towards the back of the image having occurred prior to delamination growth (contrarily to the ply split in the foreground) did not lead to delamination migration. In-plane shear fibre failure of the third ply (Figure 13) was observed between a narrow zone that was bounded by ply splits A-A' and B-B' (site 5 in Figure 11).

Based on these observations, the detailed failure sequence (Figure 14) for Specimen H2 (defect at the +65°/-25° ply interface) was deduced. This was very similar to that of the Baseline configuration (Figure 6). Firstly (Figure 14a)) ply splits in the third layer (+65°) had developed both before and after (Figure 12) delamination growth. Through one ply split delamination changed ply interface to the +20°/+65° ply interface (Figure 14b) and the local growth direction changed to match the backward ply (+65°). After ply splitting and delamination growth, the ply splits and the insert tip stress concentrator promoted the formation of in-plane shear fibre failure (Figure 14c).

### *4.3. Observations on Specimen E2 (+80˚/-10˚ ply interface)*

Specimen E2 (+80°/-10°) had a stacking sequence which had been rotated by +35° as compared to that of the Baseline (i.e. $[-55^{\circ}/+35^{\circ}/+80^{\circ}/-10^{\circ}]_{4S}$), and is shown in Figure 15. However, unlike the Baseline, the delamination surface in Specimen E2 (Figure 15b) was entirely contained within the original defect plane (i.e. between plies three and four). It was notable that the delamination had propagated asymmetrically, having grown 35 mm on one

side and 10 mm to the other: the C-scan presented in Figure 15a corresponds to the former side.

As can be seen in Figure 15, a ply split had developed in the third (+80˚) ply tangentially to the lowermost part of the insert boundary (B-B' in Figure 15c). However, its location was far from the delamination growth initiation sites at approximately the axial boundary of the defect. Therefore, unlike in the Baseline (Specimen I), no interaction between the third ply splitting and delamination growth had occurred.

Tangential to the transverse boundary of the defect, a ply split of the fourth (-10˚) ply had developed (A-A' in Figure 15c). From the middle of this ply split, fibres micro-buckled leading to a compression failure that extended away from the embedded defect, as shown in Figure 16 (site 6 in Figure 15c). From the continuity of the fracture morphology at this site, it was inferred that the delaminated surfaces had been generated prior to formation of the ply splitting in the fourth ply. The compression failure was inferred to have initiated at the ply split, since it was only present on one side of this ply split surface. Similarly to the Baseline, the compression failure was located at a load bearing ply.

As shown in Figure 17, the growth sequence in Specimen E2 (defect located at the +80°/-10° ply interface) differed from that of the Baseline (defect located at the +45°/-45° ply interface) since there was no significant delamination migration in Specimen E2. Instead the delamination had grown at the original defect plane whilst some ply splitting of the fourth (-10°) ply had developed (Figure 17a and Figure 17b). Consequently, compression failure of the fourth ply (-10°) had extended away from the starter defect, initiating at these ply splits.

### *4.4. Observations on Specimen C (+87˚/-3˚ ply interface)*

Specimen C ($[-48^{\circ}/+42^{\circ}/+87^{\circ}/-3^{\circ}]_{4S}$) with a defect at the +87°/-3° ply interface had a stacking sequence which had been rotated by +42˚ with respect to the Baseline configuration. As

shown in Figure 18, this specimen presented similarities with Specimen E2 (+80°/-10° ply interface), by which it only differed in orientation by +7˚. As with Specimen E2, Specimen C also presented delamination in the original defect plane and fibre failure of the fourth ply. However, upon closer examination, it was apparent that there was a different failure sequence. Unlike specimen E2, ply splitting of the fourth ply (-3˚), which are shown as splits A-A' and B-B' in Figure 18b, was after the translaminar compression failure of this ply. In Figure 19 (site 8 in Figure 18c), the intersections between these -3° ply splits and the translaminar compression failure are shown. It was apparent that the compression failure was continuous across the ply splits, from which it was inferred that the compression failure had occurred first.

The sequence of events for Specimen C (defect at the +87°/-3° ply interface) is illustrated in Figure 20. . Although ply splits developed in the third ply (+87°), the delamination remained at the original ply interface (Figure 20a). This is similar to the observations of Specimen E2 (Figure 15c). Once the fourth (-3˚) ply had been exposed by the delamination, the lack of through-thickness support on this loading ply had promoted micro-buckling, which had propagated away from the starter defect (Figure 20b). Consequently, from this compression failure, delamination had grown between the fourth and fifth plies (Figure 20c). Finally, ply splits had developed in the fourth (-3˚) ply (Figure 20c).

### *4.5. Observations on Specimen B (90˚/0˚ ply interface)*

Specimen B (defect located at the 90°/0° ply interface) was the only specimen that did not exhibit substantial local buckling prior to delamination therefore the observations from this specimen were limited. As can be seen in Figure 21, the delamination had propagated across the entire specimen upon global buckling (Figure 21a) and delamination migration or ply splitting had not occurred (Figure 21b).

## 5. Discussion

### *5.1. Mechanical Test Results*

No significant dependency on the stacking sequence was observed for any of the parameters studied (local and global buckling load and delamination growth strain). Also, the two configurations (+80°/-10° and +65˚/-25˚) with two specimens tested (E, E2 and H1, H2) exhibited too large a scatter to infer any dependence on the stacking sequence. The scatter observed during the 1$^{st}$ load step has been previously reported in the literature [20] as being caused by the PTFE film adhering to substrate. For the subsequent load steps, the scatter could be due to the fact that the load steps were dictated solely by acoustic and visual cues on the specimen indicating delamination growth. Although it was attempted to eliminate the effect of the load steps by taking into account the measured delamination growth and the load reached during the previous load steps the scatter remains significant. However, a general interpretation of the results is still possible. The global buckling load decreased as the maximum load of the previous load step increased (Figure 5). Even if the global buckling load was reduced in subsequent load steps, the effect of delamination growth on the global buckling load was not clear, suggesting that the reduction in global performance could be dominated by other failure modes.

### *5.2. Fractographic Analysis*

While there are discrepancies between the results for the repeated specimens in terms of buckling load and delamination growth onset, the growth mechanisms are thought to have a higher degree of reproducibility as shown on the C-scans of the repeated specimens H1 and H2 in Figure 4. Based on the fractographic observations, the failure sequence and growth directions for Specimens I, H2, E2, and C are summarized in Figure 10, Figure 14, Figure 17 and Figure 20, respectively. It can be summarised as follows: the region above the pre-inserted defect buckled and formed a blister. Due to the high-bending strains at the insert

boundary and in-plane shear from the unbalanced delaminated layers, ply-splits started at the third ply tangential to the insert boundary and grew away from the insert. The intralaminar failure had a larger shear component in specimen I and H2 (Figure 12), while in specimen C it was mainly transverse tension (Figure 19). When the third ply was approximately orientated at 90˚ (E2 and C, +80˚/-10˚ and +87˚/-3˚ interfaces), the direction of the induced local buckling promoted the formation of ply splits at the axial boundary of the insert (Figure 1). When the third ply was close to +45˚ (H2 and I, +45˚/-45˚ and +65˚/-25˚ interfaces, respectively) the position of the ply splits (Figure 10, Figure 14, Figure 17 and Figure 20) shifted towards the transverse boundary of the insert. Delamination migration occurred through these pre-existing ply splits. However, the sole presence of the ply split was not enough to promote complete migration. This is analogous to the findings of Pernice et al. [9,17] where several migration "attempts" were observed before delamination migration was completed.

From the stress state at the crack tip at the axial boundary of the defect it can be deduced that migration will be dictated by the backward uppermost ply (third) at the delaminated interface [23]. In a similar mechanism as described by Canturri et al. [12], migration did not occur when the uppermost ply (third) was aligned to the global growth (E2, C and B, +80˚, +87˚ and 90˚). For specimens H2 and I, (upper ply being +45˚ and +65˚ respectively) this was not the case. The delamination then migrated via ply splitting until the uppermost ply of the delaminated interface matched the growth direction.

After the delamination initiation and growth the generated delaminated surfaces lacked out-of-plane support. The fibres in the load carrying plies (i.e. 0˚ or close to this orientation) which were as such free surfaces, microbuckled and ultimately failed. Compression failure had started near the delamination initiation site and had then propagated away from the insert. Fibre microbuckling was observed in specimens E2, C and I. For specimens where there was

no predominant load carrying ply exposed, such as in specimen H2, compression failure did not develop. Similarly specimens E2 and C did not have significant load carried within the first three plies and therefore the compression failure was located within the fourth ply (-10˚ and -3˚, respectively). This compression failure was thought to have been contained by the ply splits and propagated only as far as the delamination reached.

To summarise, the local growth direction was dictated by the direction of the fibres at the upper face of the delaminated interface. Delamination migration occurred through pre-existing ply splits that had developed in the vicinity of delamination boundary. The location of these ply splits was dictated by the stacking sequence of the delaminated plies. As a late event, if delamination had developed at an interface with plies aligned with the load, these were likely to have exhibited fibre micro-buckling leading to compressive failure. In summary, the overall failure mechanisms were strongly influenced by the stacking sequence.

## 6. Concluding Remarks

A fractographic study into the influence of ply interface orientation on delamination growth mechanisms from embedded defects was undertaken. 11 composite panels (eight stacking sequences) with an embedded delamination were tested in compression until delamination growth was observed. The influence of the stacking sequences on the delamination growth and panel buckling were examined. From the eight stacking sequences tested, four stacking sequences were studied in detail via fractography and the modes and sequences of failure deduced. Delamination was proven to closely interact with ply splits. However, the presence of ply splitting alone was not sufficient to dictate if delamination migration would ensue. It was observed that, although macroscopically delamination migrated through a single ply split, multiple delamination migration attempts were observed close to the final delamination migration site. This resulted in limited crack branching at the vicinity of the migration step

and in a crack mostly progressing in a continuous manner elsewhere. The presence of plies parallel to the load, i.e. transverse to the delamination growth direction, promoted migration and thus inhibited the delamination growth. However, it was observed that once those plies had delaminated the load carrying plies were prone to out-of-plane microbuckling. These secondary failure modes were thought to have a greater impact on the reduction of the overall compression performance of the laminate than the advance of delamination. This study shows the importance for predictive models to not only predict the extent of the delamination but more importantly, the ply interface at which the delamination propagates. This detailed results can be used to validate those numerical models of progressive delamination growth where migration is explicitly modelled.

## 7. Acknowledgements

Torvald Linderoth and Bernt Thörnqvist are hereby thanked for their skilful contribution in the experimental work, Soren Nilsson is thanked for valuable technical discussions. Carla Canturri acknowledges the support of Fundacio Credit Andorra to conduct this work during her stay at Imperial College London.

## 8. References

[1] Sridharan S. Delamination behaviour of composites. Woodhead Pub; 2008.

[2] Nilsson K-F, Asp LE, Sjögren A. On transition of delamination growth behaviour for compression loaded composite panels. Int J Solids Struct 2001;38:8407–40. doi:10.1016/S0020-7683(01)00114-7.

[3] Rhead AT, Butler R, Hunt GW. Compressive strength of composite laminates with delamination-induced interaction of panel and sublaminate buckling modes. Compos Struct 2017;171:326–34. doi:10.1016/j.compstruct.2017.03.011.

[4] Riccio A, Pietropaoli E. Modeling damage propagation in composite plates with embedded delamination under compressive load. J Compos Mater 2008;42:1309–35. doi:10.1177/0021998308092199.

[5] Chai H, Knauss WG, Babcock CD. Observation of damage growth in compressively loaded laminates. Exp Mech 1983;23:329–37. doi:10.1007/BF02319260.

[6] Suemasu H, Tanikado Y. Damage growth behavior and interlaminar fracture resistance of CFRP laminates under shear fracture mode. Adv Compos Mater 2015;24:451–66. doi:10.1080/09243046.2014.914998.

[7] Pavier MJ, Clarke MP. Experimental techniques for the investigation of the effects of impact damage on carbon-fibre composites. Compos Sci Technol 1995;55:157–69. doi:10.1016/0266-3538(95)00097-6.

[8] Greenhalgh E, Meeks C, Clarke A, Thatcher J. The effect of defects on the performance of post-buckled CFRP stringer-stiffened panels. Compos Part A Appl Sci Manuf 2003;34:623–33. doi:10.1016/S1359-835X(03)00098-8.

[9] Pernice MF, De Carvalho N V., Ratcliffe JG, Hallett SR. Experimental study on delamination migration in composite laminates. Compos Part A Appl Sci Manuf 2015;73:20–34. doi:10.1016/j.compositesa.2015.02.018.

[10] Ratcliffe JG, De Carvalho N V. Investigating Delamination Migration in Multidirectional Tape Laminates. NASA/TM-2014-218289 2014.

[11] Hu XF, Chen BY, Tirvaudey M, Tan VBC, Tay TE. Integrated XFEM-CE analysis of delamination migration in multi-directional composite laminates. Compos Part A Appl Sci Manuf 2016;90:161–73. doi:10.1016/J.COMPOSITESA.2016.07.007.

[12] Canturri C, Greenhalgh ES, Pinho ST. The relationship between mixed-mode II/III

delamination and delamination migration in composite laminates. Compos Sci Technol 2014;105. doi:10.1016/j.compscitech.2014.10.001.

[13] Li X, Chen J. An extended cohesive damage model for simulating multicrack propagation in fibre composites. Compos Struct 2016;143:1–8. doi:10.1016/J.COMPSTRUCT.2016.02.026.

[14] Canturri C, Greenhalgh ES, Pinho ST, Ankersen J. Delamination growth directionality and the subsequent migration processes - The key to damage tolerant design. Compos Part A Appl Sci Manuf 2013;54. doi:10.1016/j.compositesa.2013.07.004.

[15] Gong Y, Zhang B, Hallett SR. Delamination migration in multidirectional composite laminates under mode I quasi-static and fatigue loading. Compos Struct 2018;189:160–76. doi:10.1016/J.COMPSTRUCT.2018.01.074.

[16] Gong Y, Zhang B, Mukhopadhyay S, Hallett SR. Experimental study on delamination migration in multidirectional laminates under mode II static and fatigue loading, with comparison to mode I. Compos Struct 2018;201:683–98. doi:10.1016/J.COMPSTRUCT.2018.06.081.

[17] McElroy M, Jackson W, Pankow M. A biaxial-bending test to observe the growth of interacting delaminations in a composite laminate plate. Proc. 31st ASC Tech. Conf., Williamsburg, Virginia: 2016.

[18] Greenhalgh ES. Characterisation of mixed-mode delamination growth in carbon–fibre composites. PhD Thesis, Imperial College London, 1998.

[19] Cytec. Cycom 950-1 Epoxy Prepreg 2012. http://www.cytec.com/sites/default/files/datasheets/CYCOM_919_111510.pdf (accessed January 12, 2018).

[20] Nilsson K-F, Asp LE, Alpman JE, Nystedt L. Delamination buckling and growth for delaminations at different depths in a slender composite panel. Int J Solids Struct 2001;38:3039–71. doi:10.1016/S0020-7683(00)00189-X.

[21] Greenhalgh ES. Failure Analysis and Fractography of Polymer Composites (Google eBook). Woodhead Pub; 2009.

[22] Nilsson S. Compression test of composite panels with embedded delaminations. Flygtek Försöksanstalten (The Aeronaut Res Inst Sweden) 2000;TN:74.

[23] Greenhalgh ES. Failure analysis and fractography of polymer composites. Woodhead Pub; 2009.

Tables

Table 1 Stacking sequence and starter defect ply interface for the embedded defect specimens.

| Panel*† | Stacking sequence | Defect Interface |
|---|---|---|
| A | $[+45^{\circ}/-45^{\circ}/0^{\circ}/90^{\circ}]_{4s}$ | 0˚/90˚ |
| **B** | $\mathbf{[-45^{\circ}/+45^{\circ}/90^{\circ}/0^{\circ}]_{4s}}$ | **90˚/0˚** |
| **C** | $\mathbf{[-48^{\circ}/+42^{\circ}/+87^{\circ}/-3^{\circ}]_{4s}}$ | **87˚/-3˚** |
| D | $[-50^{\circ}/+40^{\circ}/+85^{\circ}/-5^{\circ}]_{4s}$ | 85˚/-5˚ |
| E1 and **E2** | $\mathbf{[-55^{\circ}/+35^{\circ}/+80^{\circ}/-10^{\circ}]_{4s}}$ | **80˚/-10˚** |
| F | $[-60^{\circ}/+30^{\circ}/+75^{\circ}/-15^{\circ}]_{4s}$ | 75˚/-15˚ |
| G | $[-75^{\circ}/+25^{\circ}/+70^{\circ}/-20^{\circ}]_{4s}$ | 70˚/-20˚ |
| H1 and **H2** | $\mathbf{[-70^{\circ}/+20^{\circ}/+65^{\circ}/-25^{\circ}]_{4s}}$ | **65˚/-25˚** |
| **I** | $\mathbf{[90^{\circ}/0^{\circ}/+45^{\circ}/-45^{\circ}]_{4s}}$ | **45˚/-45˚** |

* Note the defect was located between the third and fourth plies for all specimens

†Specimens examined using fractography are indicated in bold

Table 2 Maximum loads, delamination strains, global and local buckling loads for the embedded delamination specimens.

| Specimen | Ply interface | Maximum load (kN) | Delamination initiation strain (με) | Global buckling Load (kN) | Local buckling load (kN) |
|---|---|---|---|---|---|
| A | 0˚/90˚ | -80.4 | -12400 | -75.1 | -33 |
| B* | 90˚/0˚ | -75.5 | -13800 | - * | -36 |
| C | 87˚/-3˚ | -70.3 | -12700 | -70.4 | -33 |
| D | 85˚/-5˚ | -71.2 | -13100 | -70.1 | -40 |
| E1 | 80˚/-10˚ | -75.5 | -10700 | -74.8 | -21 |
| E2 | 80˚/-10˚ | -70.7 | -10800 | -68.7 | -29 |
| F | 75˚/-15˚ | -72.8 | -7900 | -71.5 | -23 |
| G | 70˚/-20˚ | -73.9 | -8800 | -73.5 | -30 |
| H1 | 65˚/-25˚ | -71.0 | -11600 | -69.6 | -32 |
| H2 | 65˚/-25˚ | -75.3 | -9600 | -74.9 | -17 |
| I | 45˚/-45˚ | -79.1 | -10500 | -77.9 | -25 |

* Delamination growth occurred before global buckling

Figures

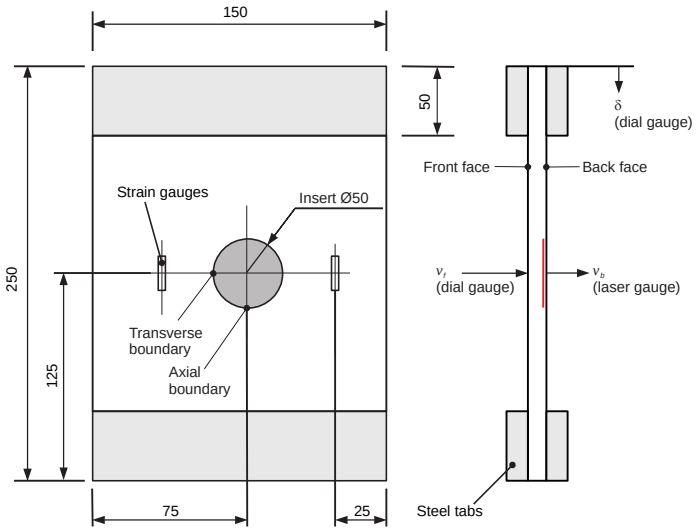


Figure 1 Specimen dimensions and instrumentation.

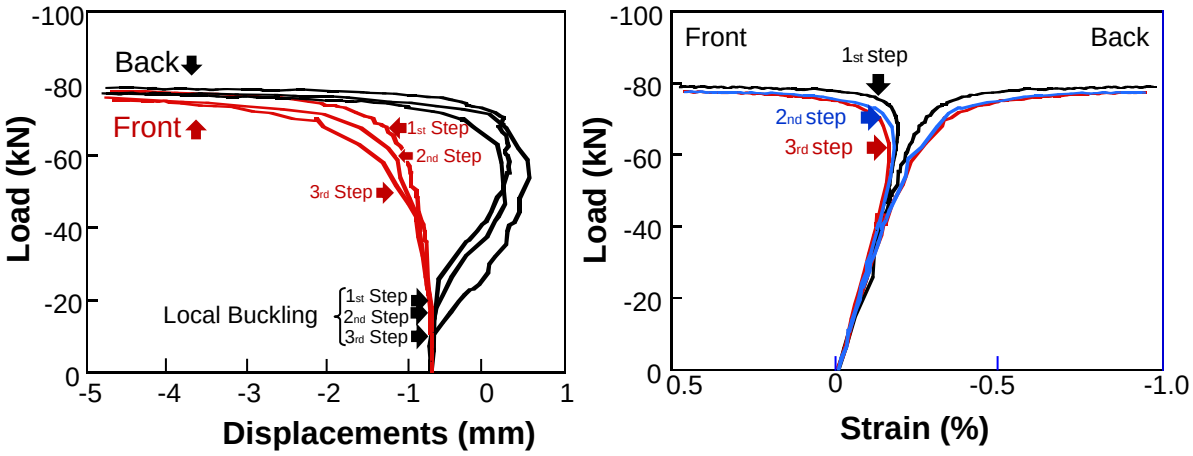


a) b)

Figure 2 Representative responses of the three load steps of a) laser gauge out-of-plane displacement and b) strain gauges in-plane compressive strains on Specimen I (defect at the +45˚/-45˚ ply interface).

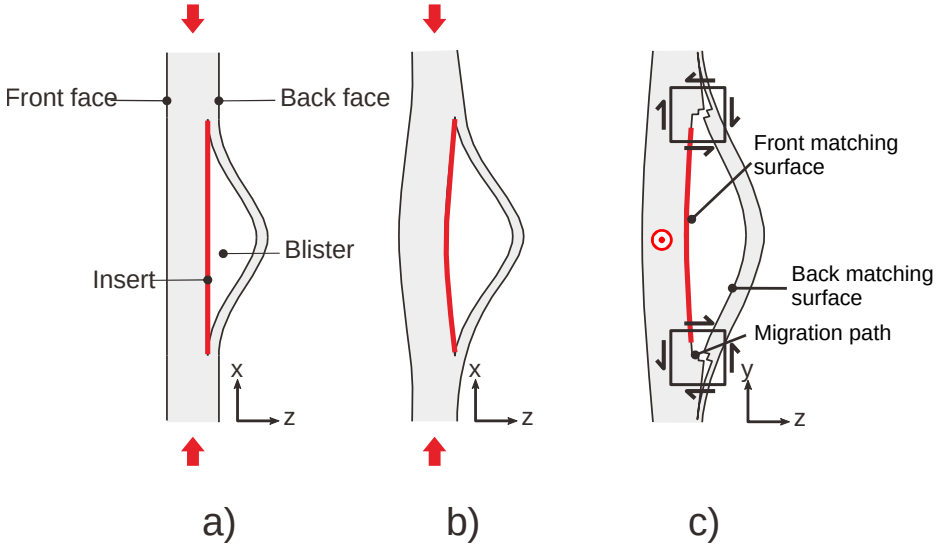


Figure 3 Damage growth mechanism of an embedded delamination with a) local buckling, b) global buckling and c) local-global buckling and delamination migration at the transverse boundary.

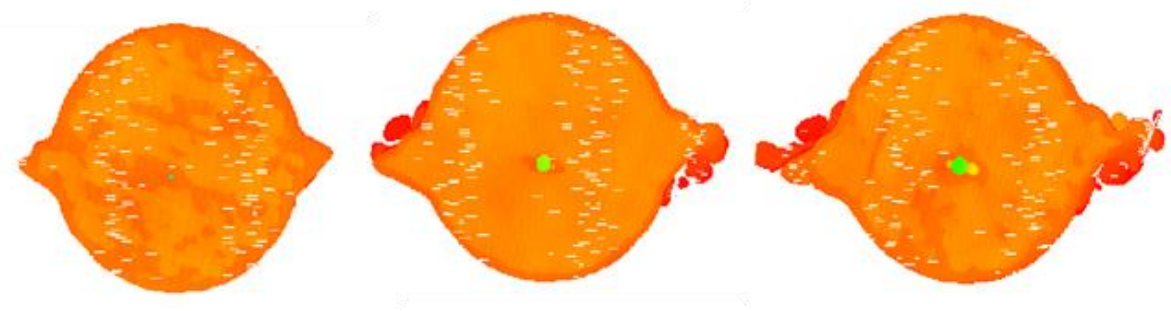

a)

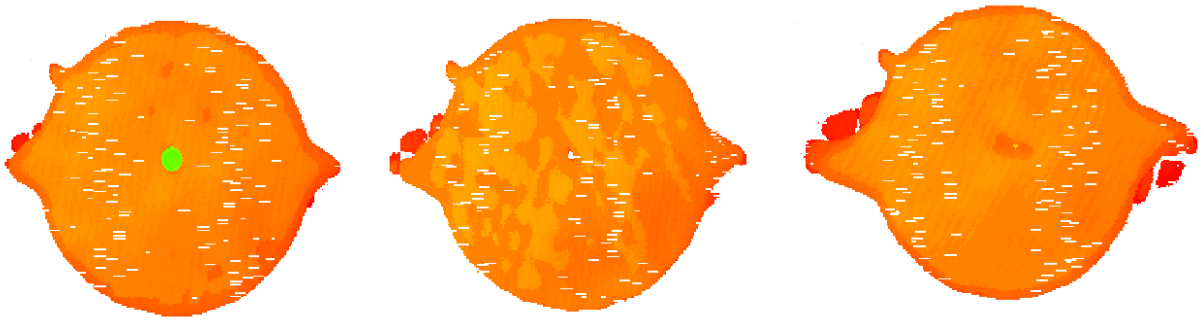

b)

Figure 4 Representative time of flight C-scans between interrupted tests of Specimen a) H1 and b) H2 (defect at the +65˚/-25˚ply interface).

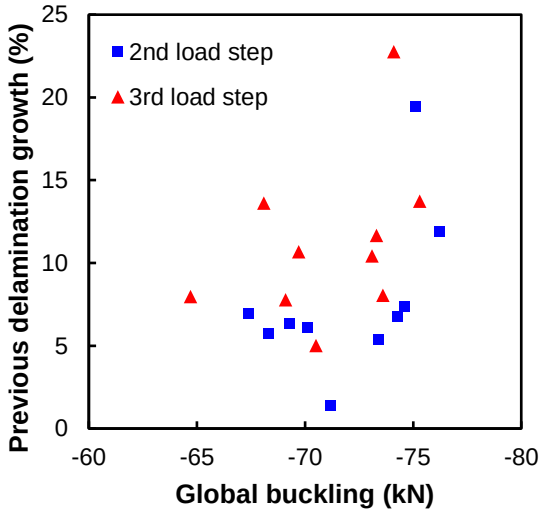


a)

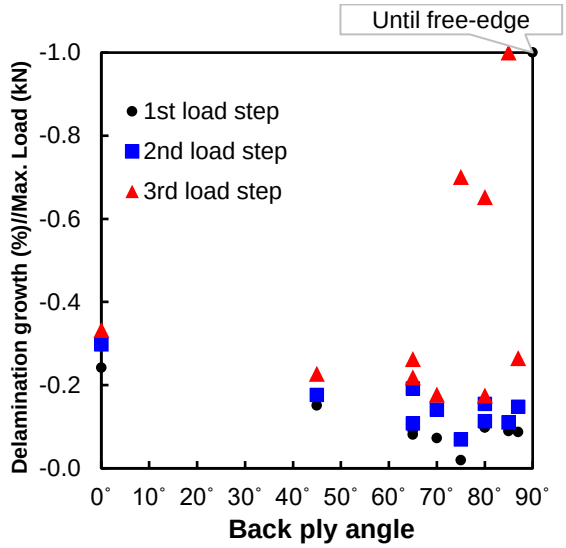


b)

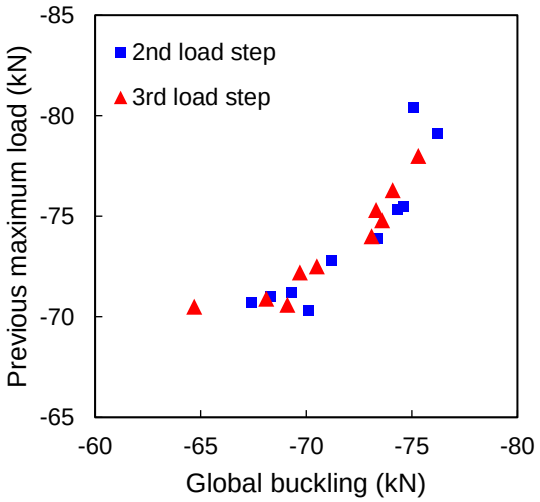


c)

Figure 5 a) Effect of the extent of the pre-existing delaminated area on global buckling; b) Effect of the back ply angle on the growth of the delaminated area and c) Effect of the maximum load on the global buckling behaviour.

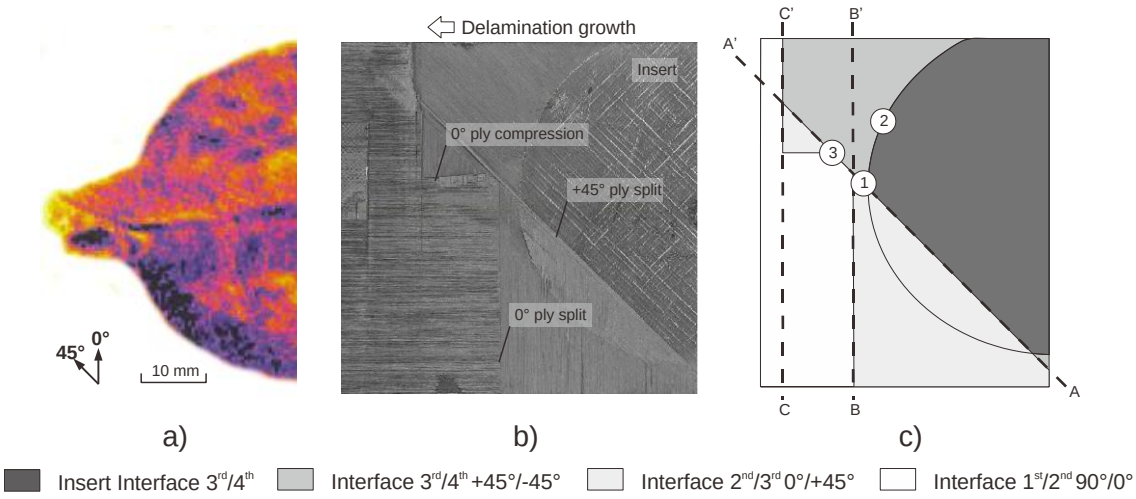


Figure **6** a) C-scan, b) front fracture surface and c) schematic showing the positions of the subsequent images from Specimen I (defect at the +45˚/-45˚ ply interface).

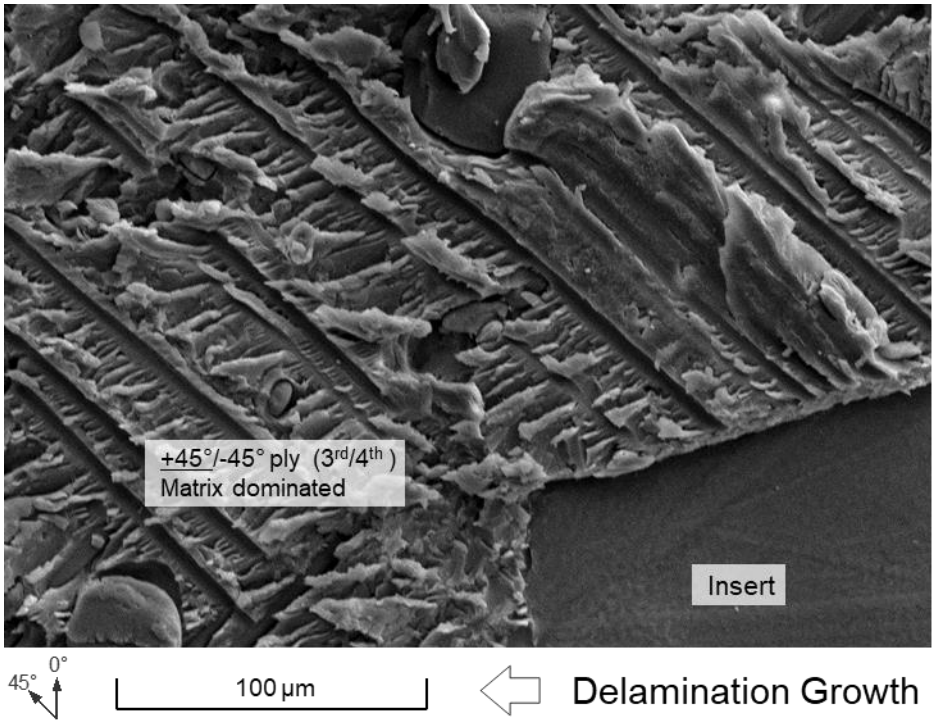


Figure 7 Delamination growth at the insert boundary of Specimen I (defect at the +45˚/ -45˚ ply interface). Site (1) in Figure **6**.

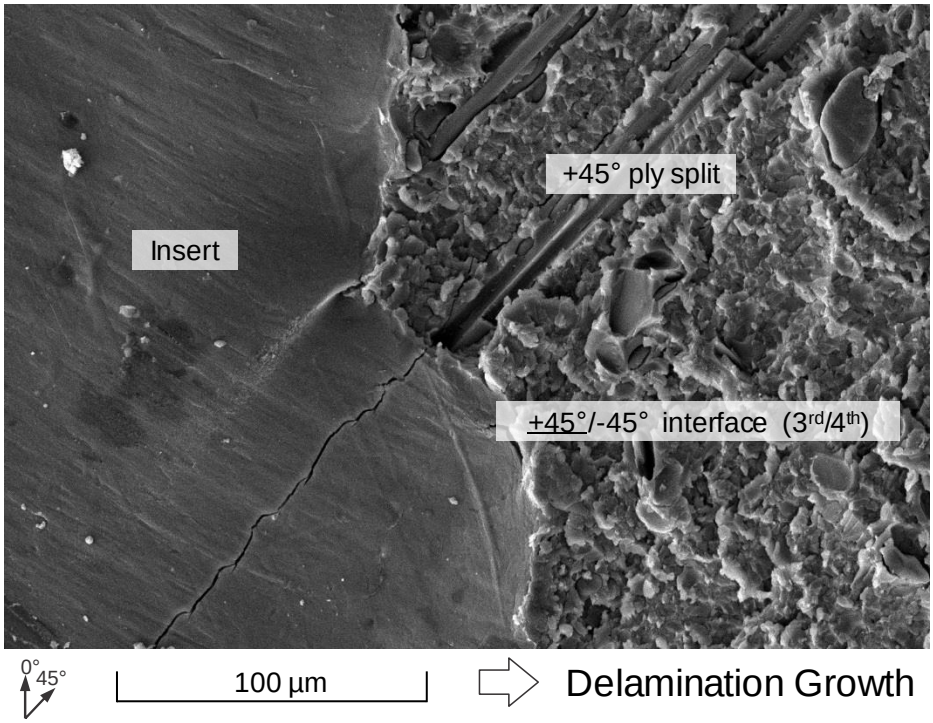


Figure 8 Ply splitting of the third ply (+45˚) of Specimen I (defect at the +45˚/ -45˚ply interface). Site (2) in Figure **6**. Note that this micrograph was taken at the back matching surface (Figure 3).

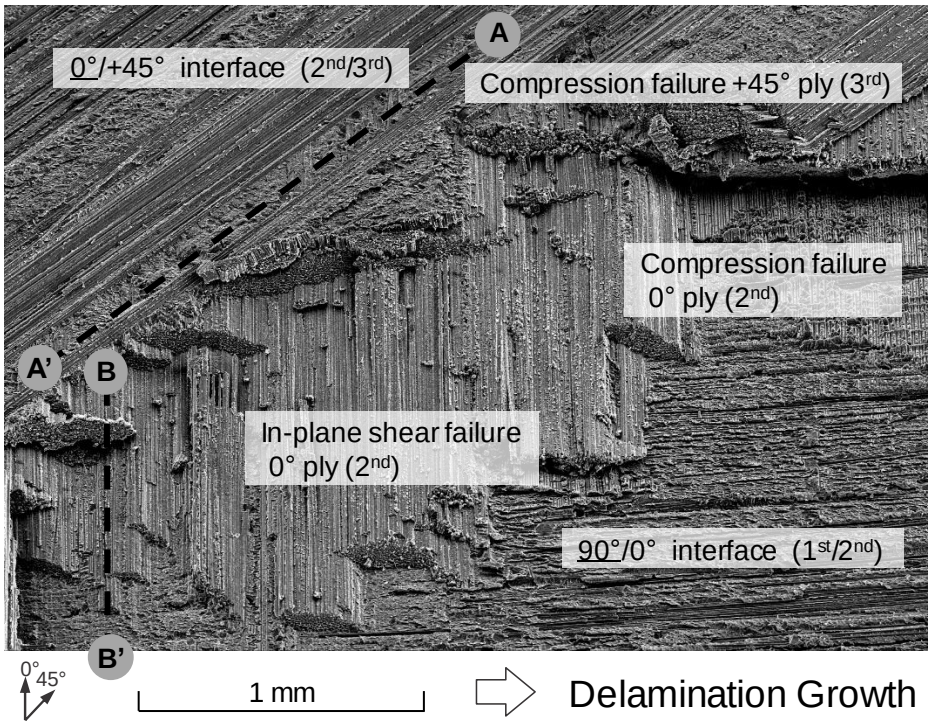


Figure 9 Compression failure of the third (+45˚) and second (0˚) plies in Specimen I (defect at the +45˚/ -45˚). Site (3) in Figure **6**. Note that this micrograph was taken at the back matching surface (Figure 3).

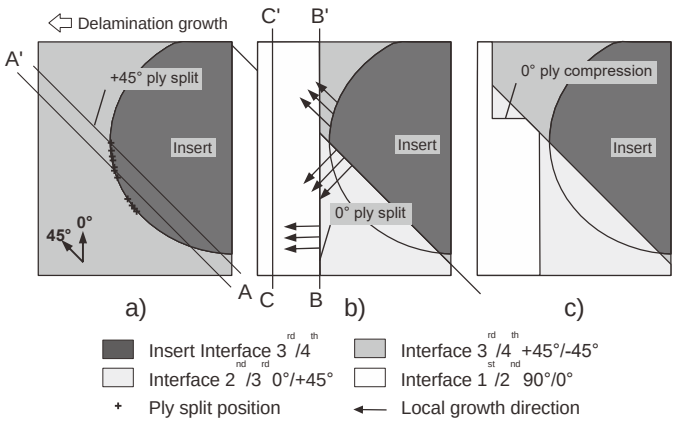


Figure 10 Failure sequence for Specimen I (Baseline) with a stacking sequence of $[90^{\circ}/0^{\circ}/+45^{\circ}/-45^{\circ}]_{4s}$ with the defect located at the +45˚/-45˚ ply interface.

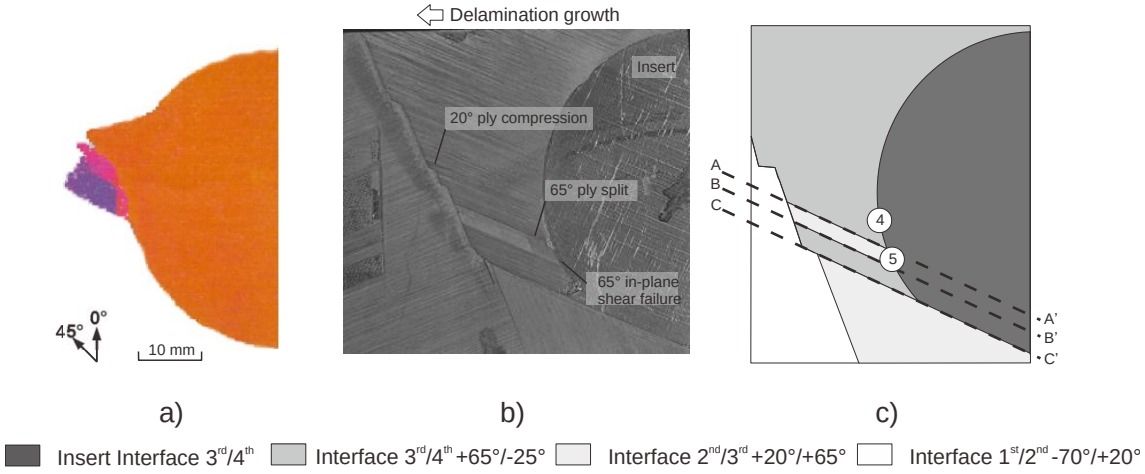


Figure 11 a) C-scan, b) front fracture surface and c) schematic showing the positions of the subsequent images of Specimen H2 (defect at the +65˚/-25˚ply interface).

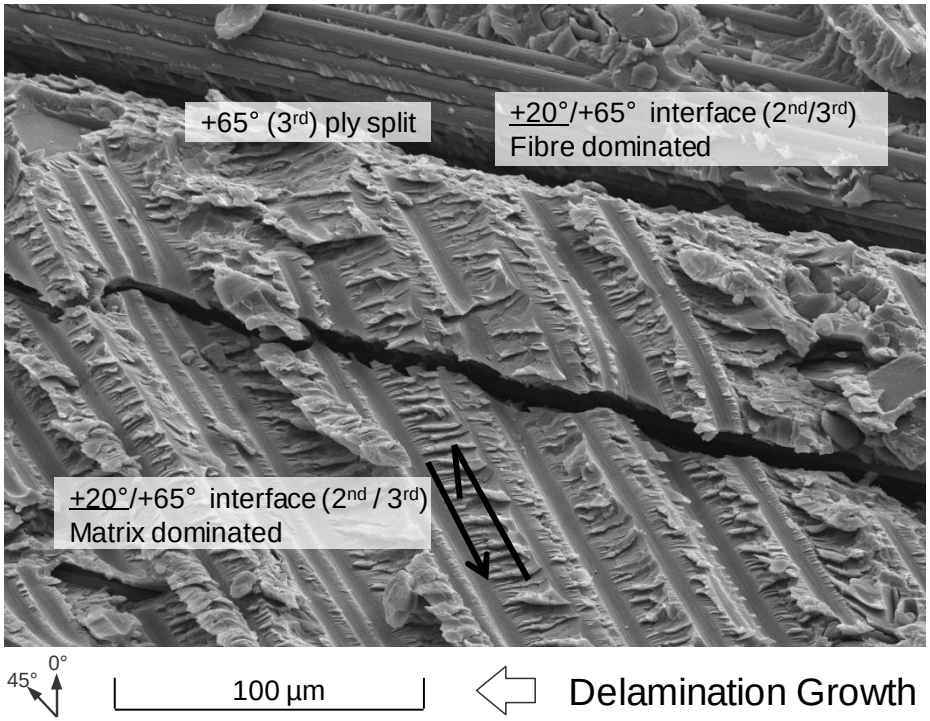


Figure 12 Ply splits of the third ply (65˚) in specimen H2 (defect at the +65˚/-25˚). Site (4) in Figure 11.

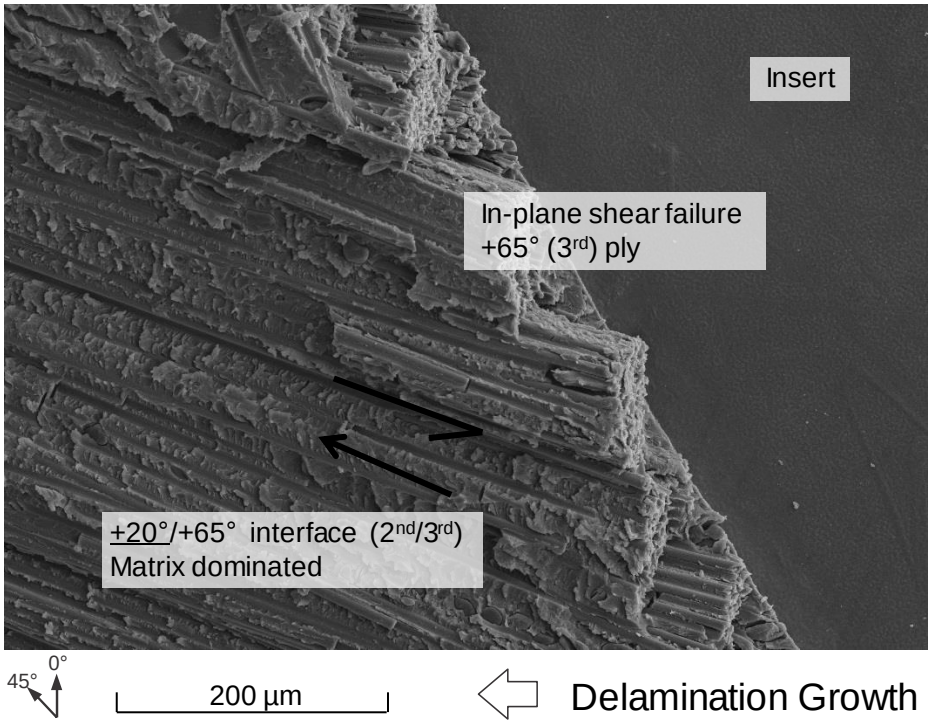


Figure **13** Boundary of the insert showing an in-plane shear failure of the third ply (65˚) in specimen H2 (defect at the +65˚/-25˚) Site (5) in Figure **11**.

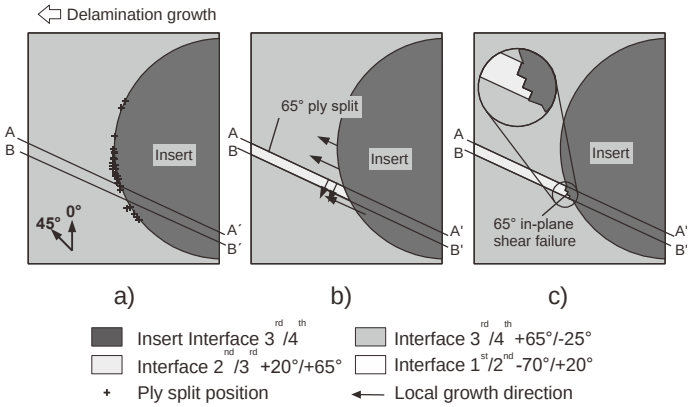


Figure 14 Failure sequence for Specimen H2 with a stacking sequence of $[-70^{\circ}/+20^{\circ}/+65^{\circ}/-25^{\circ}]_{4s}$ and the defect located at the +65˚/-25˚ ply interface.

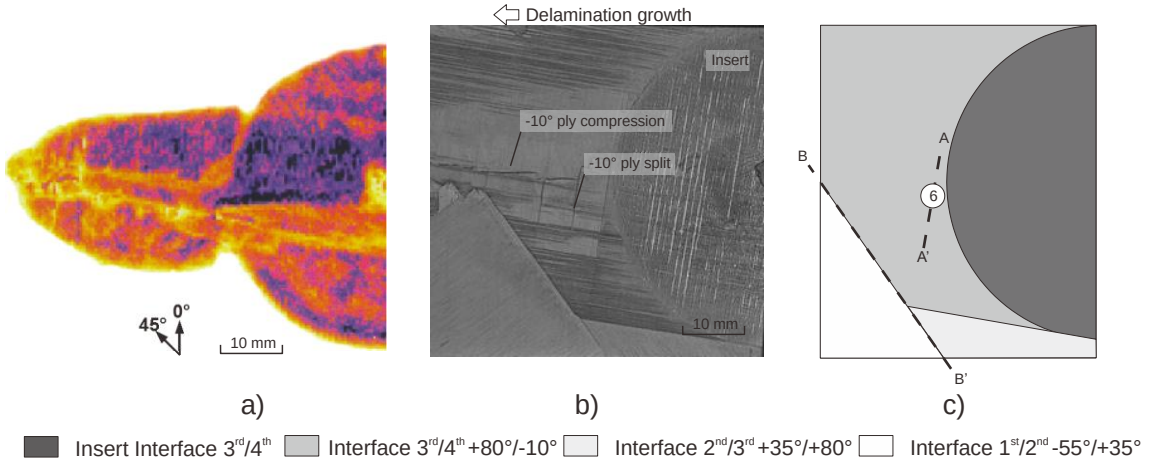


Figure **15** a) C-scan, b) front fracture surface and c) schematic showing the positions of the subsequent images of Specimen E2 (defect at the +80˚/-10˚ ply interface).

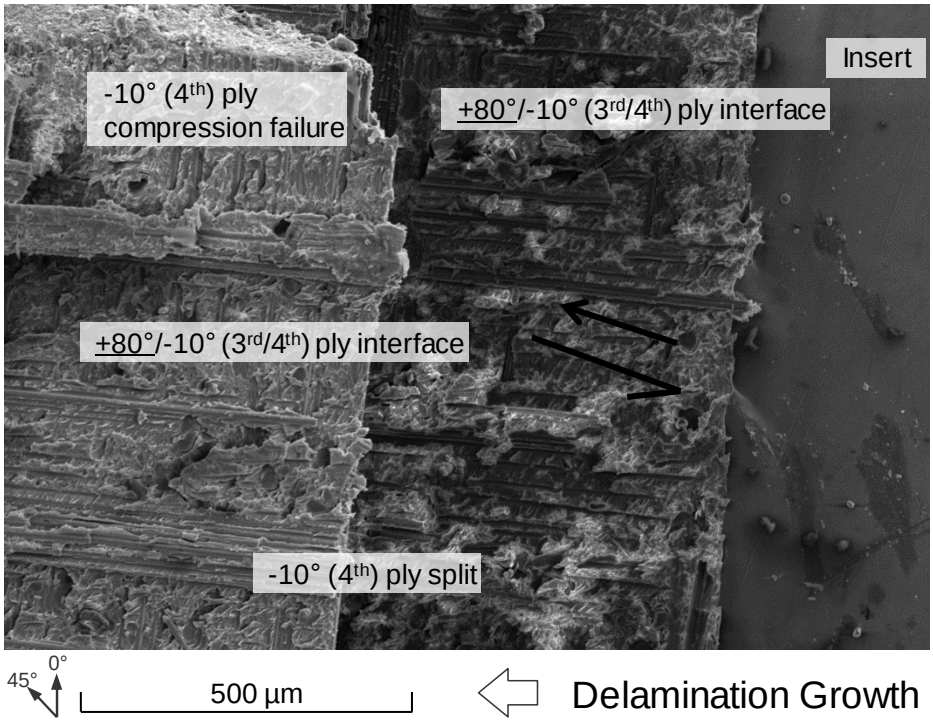


Figure 16 Boundary of the insert in Specimen E2 (defect at the +80˚/-10˚) showing compression failure and ply splitting of the fourth ply (-10˚). Site (6) in Figure **15**.

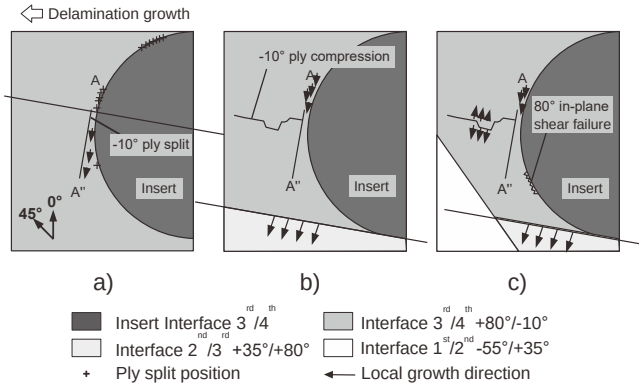


Figure 17 Failure sequence Specimen E2 with a stacking sequence of $[-55^{\circ}/+35^{\circ}/+80^{\circ}/-10^{\circ}]_{4s}$ and the defect located at the +80˚/-10˚ ply interface.

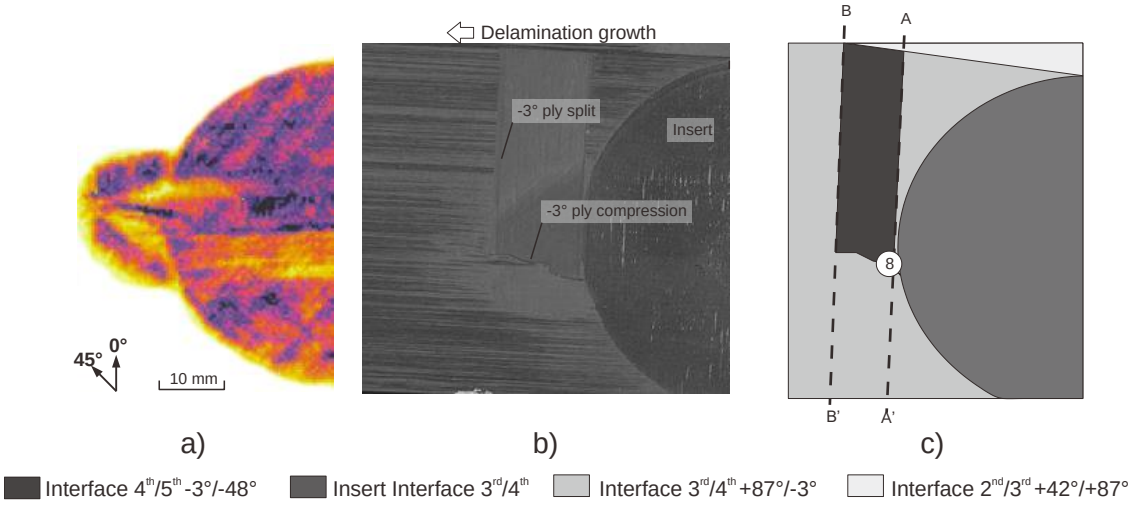


Figure 18 a) C-scan, b) front fracture surface and c) schematic showing the positions of the subsequent images of Specimen C (defect at the +87˚/-3˚ ply interface).

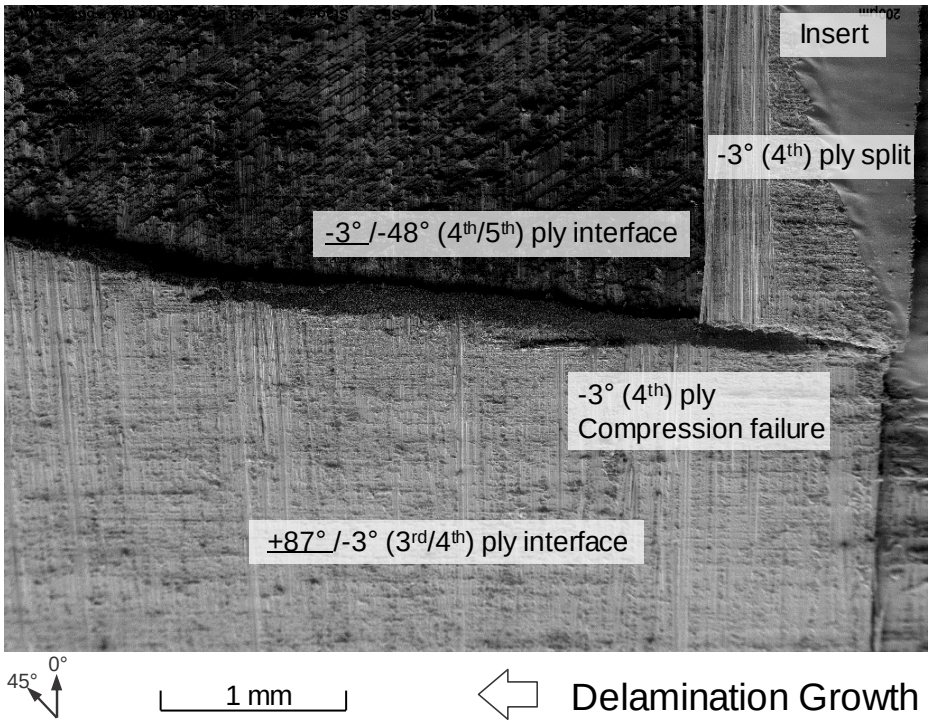


Figure 19 Surface detail of the third ply (+87˚) in Specimen C (defect at +87˚/-3˚). Site (8) in Figure 18.

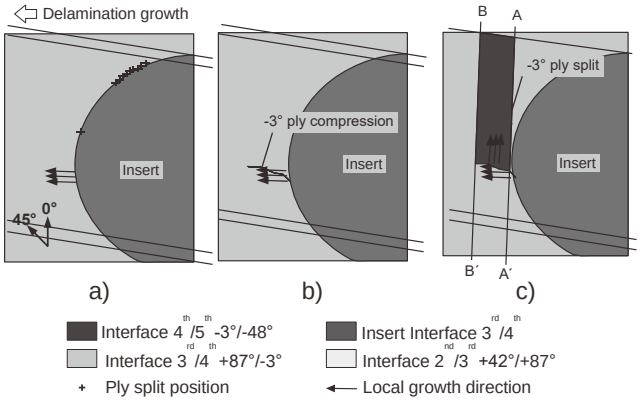


Figure 20 Failure sequence Specimen C with a stacking sequence of $[-48^{\circ}/+42^{\circ}/+87^{\circ}/-3^{\circ}]_{4s}$ and the defect located at the +87˚/-3˚ ply interface.

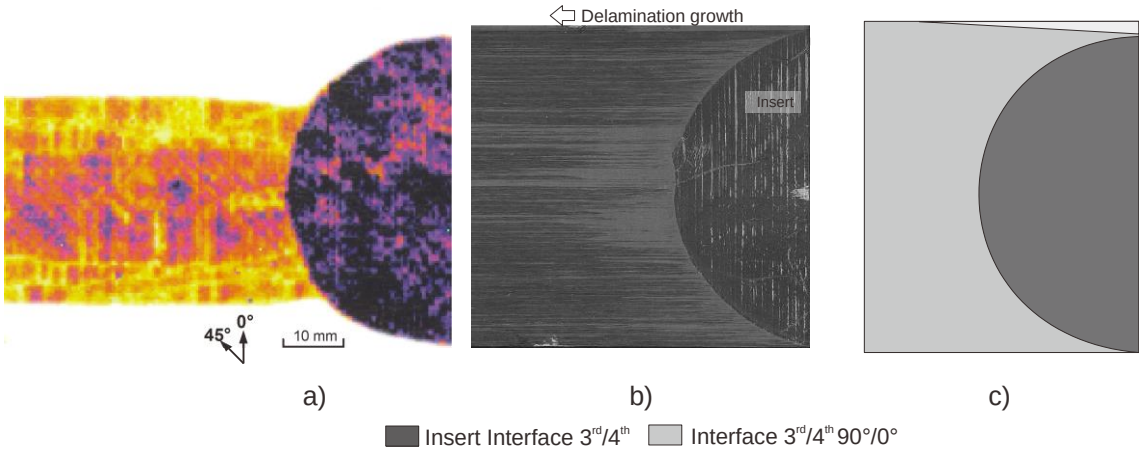


Figure 21 a) C-scan, b) front fracture surface and c) schematic showing the positions of the subsequent images of Specimen B (defect at the +90˚/-0˚ ply interface).